



Senescence screening of mesenchymal stromal cells by morphology-based deep learning senescence analysis

Liudi Wang^{a,1}, Haijie Zhang^{b,1}, Jianwei Chen^b, Xiangtian Xue^b, Yang Chen^b, Tianyun Gao^a, Yuanyuan Xie^a, Xiaoli Mai^{c,*}, Bin Wang^{a,*}

^a Department of Clinical Stem Cell Center, Nanjing Drum Tower Hospital, Affiliated Hospital of Medical School, Nanjing University, 321 Zhongshan Road, Nanjing 210008, People's Republic of China

^b Laboratory of Image Science and Technology, Southeast University, Nanjing, 210096, People's Republic of China

^c Department of Radiology, Nanjing Drum Tower Hospital, Affiliated Hospital of Medical School, Nanjing University, Nanjing 210008, People's Republic of China

ARTICLE INFO

Keywords:

Umbilical Cord Mesenchymal Stromal Cells (UCMSCs)
Bone Marrow Mesenchymal Stromal Cells (BMMSCs)
Stem cell therapy
Image analysis
Deep learning
Conventional Neural Network (CNN)
ResNeXt

ABSTRACT

Mesenchymal stromal cells (MSCs) therapy has emerged as a new approach for regenerative medicine. However, with the expansion of MSCs, passaging-induced *in vitro* senescence inevitably leads to impaired cellular quality and reduced their regenerative capacity, thereby limiting therapeutic efficacy. Until now, there is no quick and effective method monitoring the senescence of clinic-grade MSCs to ensure their quality before clinic use. Here, we introduced a morphology-based deep learning senescence analysis system to identify the passage number of MSCs to evaluate the senescence state of MSCs from pre-trained ResNeXt network. We used some specific molecular markers to identify aged MSCs, which exhibited flat and hypertrophic senescent-like morphology, decreased proliferation ability and immunomodulatory function. Especially, we used the expression of Ki67, RPS6, and β -galactosidase (β -gal) to identify senescent cells with increasing cell generations. Simultaneously, we used the ResNeXt network as the classification network, which could analyze the images of human umbilical cord mesenchymal stromal cells (HUCMSCs) and human bone marrow mesenchymal stromal cells (HBMMSCs) automatically. We found that culture generation could induce *in vitro* natural senescence of HUCMSCs, exhibiting flat and hypertrophic morphology, decreased proliferation ability and immunomodulatory function, increased aging markers including Ki67(+), pRPS6(+), SA- β -gal(+), P16, P21, and p53 expressions. Thus the number of cell passage represents the aging degree of cells. Subsequently, we successfully evaluate the senescence state of MSCs from pre-trained ResNeXt network optimized for classifying the natural cellular senescence. Our system identified the passage number and types of MSCs with high accuracy.

1. Introduction

Mesenchymal stromal cells (MSCs), a type of adult stromal cells derived from the mesoderm, have self-renewal, multi-differentiation potentials, and immune regulation capabilities [1–4]. MSCs can be isolated from various tissues such as bone marrow, adipose, umbilical cord, amniotic membrane, placenta, gingiva, and dental pulp [5–8]. Compared with other tissue-derived MSCs, human umbilical cord-derived mesenchymal stromal cells (HUCMSCs) have a wide range of clinical application prospects in regenerative medicine and tissue engineering due to their simple isolation, high purity, quick expansion, and excellent immunomodulatory function [9–11]. It is well known that

aging of cultured MSCs, same as other cells, will gradually step into senescence as the number of passages increases during proliferation process.

The hallmarks of senescent cells encompass alterations in chromatin structure, cessation of proliferation, metabolic reprogramming, upregulation of anti-apoptotic pathways, accumulation of damaged macromolecules, and genomic instability [12]. Characterizing and identifying senescent cells has posed a longstanding challenge due to the absence of specific markers unique to cellular senescence. Consequently, reliance on a single marker is insufficient for defining the senescent state, as these markers may also be present in other cellular conditions. Therefore, the use of a combination of multiple markers is essential for the accurate

* Corresponding authors.

E-mail addresses: maixl@nju.edu.cn (X. Mai), wangbin022800@126.com (B. Wang).

¹ These authors contributed equally to this work.

identification of senescent cells. MSCs at early passage are small and have fibroblast-like morphology while senescent MSCs at late-passage appear relatively hypertrophic and flattened forms during expansion and culture *in vitro* [13–15]. The enlargement of senescent cells into hypertrophic cell morphology is often accompanied by changes in their biological characteristics [16,17].

Cellular senescence was a permanent state of cell cycle arrest that served as a response to stress or damage, leading to various intracellular phenotypic changes. Many senescent cells accumulated p21 that inhibited cyclin-dependent kinases (CDK) and activated p16 that inhibited CDK activity, resulting in sustained hypo-phosphorylation of RB family proteins, inhibited E2F transcription factors, downregulated the proliferation marker MKI67, and, subsequently cell cycle arrest [18–20]. Furthermore, activation of RB and p53 also occurred in other forms of cell cycle blockade [21].

Senescent cells can be defined as arrested cells with activated mTOR [22]. The ribosomal protein S6 (RPS6) is phosphorylated in response to mTOR activation, which serves as a marker that distinguishes between senescent and quiescent cells [23,24].

In senescent cells, both the number and size of lysosomes increased, and the increased lysosomal mass was associated with the activity of the senescence associated β -galactosidase (SA- β -gal), which increased during cellular senescence [25]. Therefore, SA- β -gal was widely used as a marker for senescent cells. By detecting the activity level of SA- β -Gal in cells, the degree of cellular senescence could be evaluated [26].

Therefore, in addition to cell morphological changes in senescent cells, specific molecular biomarkers can be used to detect cellular senescence, such as P16, P21, and p53 proteins. Simultaneously, the expression of Ki67 and ribosomal protein S6 (RPS6), as well as the assessment of β -galactosidase activity, are widely used to identify senescent cells [27,28].

A variety of culturing elements such as stressors and DNA damage could lead to senescence, constant culturing passages induced the replicative senescence due to the division potential exhaustion [29,30]. In addition, replicative senescence decreases genetic stability of cultured MSCs and aggravates the risk of cell transformation [31]. Furthermore, senescent cells could directly facilitate the tumorigenesis or promote the invasiveness and proliferation of malignant cells by releasing senescence-associated secretory phenotype (SASP) including chemokines, cytokines, and proteases [32]. Thus, the senescent MSCs will reduce the therapeutic efficacy and bring a risk of tumorigenesis to recipients when applied to clinical therapy.

Clinic-grade MSCs must meet the criteria of high quality. In previous study, we have established systematic quality assessments of manufactured MSCs for therapeutic application [33]. Because there is a tight connection of transformation and senescence, the altered functions and transformation of senescent MSCs may bring a high safety risk to recipients of cell therapies. Thus MSCs-based therapeutic products should be performed cellular quality evaluation of senescence because senescence could compromise the quality of manufactured cells and decrease their functionality. The systematic quality assessments of clinic-grade MSCs are complex and contains a combination of various evaluation methods. Until now, there are still lacking a fast screening method for quality evaluation and senescence of cultured MSCs, especially for the quick release inspection of MSCs-based therapeutic products before clinic use.

At present, Convolution Neural Network (CNN) based deep learning methods have acquired productive applications in the field of image classification [34–37]. CNN based methods extract the image features through the convolutional layer, and learns the parameters through backpropagation. In a word, the neural network can automatically learn and adjust parameters so that appropriate features can be extracted for specific tasks defined in training stage. These features may be subtle features that humans are not able to notice, or they may be extensively complex. Each cell shows a unique cellular morphology. CNN will be an alternative technique for different sources of cell morphological

identification. The development of CNN makes it possible to automatically identify the generations and types of MSCs based on phase contrast microscope images, which will be well applied in biomedical field. The accuracy of image classification by CNN has largely exceeded that of human recognition, which potentially was an efficient and highly modular network structure used for image classification in the quality assessments of clinic-grade MSCs in cell therapy.

In this study, we have developed an automated image analysis method based on the morphology of MSCs for identifying their generation number, which represented the senescence and quality of cultured MSC. We investigated whether morphological changes could accompany cell aging and recognize the generation numbers of cultured MSCs during their expansion using automated image analysis. The aim of our study was to develop and validate a tool for quick cellular quality screening based on cell morphology changes in MSCs-based therapy.

2. Methods

2.1. Isolation and culture of HUCMSCs and HBMMSCs

This study was approved by the Research Ethics Board of Nanjing Drum Tower Hospital, - Affiliated Hospital of Medical School, Nanjing University. The umbilical cord tissue ($n = 14$) was derived from normal term infants born and bone marrow ($n = 14$) were obtained from iliac crest aspirates of healthy donors in the Department of Obstetrics and Gynecology, Nanjing Drum Tower Hospital. All donors signed informed consent. The parturient had no family history of hereditary disease or infectious disease through screening examination, and the test for HBV, HCV, HIV, syphilis and other pathogens was negative. The umbilical cord tissue and bone marrow were obtained in a sterile bottle under aseptic conditions in the delivery room, and was transported to the Clinical Stem Cell Research Center at 4 °C for cell isolation and culture according to our previous publication [33].

The umbilical cord tissue was cut into about 2-cm small sections and repeatedly washed with DPBS containing 2 % penicillin streptomycin. The three blood vessels in the umbilical cord were removed carefully and residue was cut into pieces of approximately 1 mm with ophthalmic scissors, which were pasted directly onto the bottom of a 75 cm² culture flask (Corning, 430641). After 4 h, the complete medium (DMEM (Gibco,10567014) containing 10 % fetal bovine serum (Gibco, 12664025) and 100 mg/mL streptomycin and 100 U/mL penicillin (Gibco, 15140122) were gently added into culture flask, which then was placed in a 5 % CO₂ incubator at 37 °C. After 10–14 days, there will be fibroblast colony forming unit (CFU-F) around the attached tissues. The passage was performed when the cells grown to 80 %–90 % confluence (passage 0, P0). HUCMSCs were passaged from P0 to P10, and the cell morphology was captured under an inverted microscope at different generations of the HUCMSCs. To observe HUCMSCs growth, the proliferation of HUCMSCs at P2, P5, and P10 were detected using an EDU kit (RiboBio Co., Ltd.) in 12-wells plates.

Bone marrow mononuclear cells were isolated by density gradient centrifugation with human lymphocyte isolation fluid (Tianjin Haoyang Biological Co., LTD, LTS10770125) and then seeded in the complete medium (DMEM (Gibco, 10567014) containing 10 % fetal bovine serum (Gibco, 12664025), 100 mg/mL streptomycin and 100 U/mL penicillin (Gibco, 15140122). Cells were incubated in a 5 % CO₂ incubator at 37 °C. After 48 h, the complete medium was changed to discard non-adherent cells and changed 2–3 per week thereafter. After 10–14 days, there will be fibroblast colony forming unit (CFU-F). The passage was performed when the cells to 80 %–90 % confluence (P0). HBMMSCs cell morphology was captured under an inverted microscope (Olympus, Japan).

2.2. Surface marker expressions of HUCMSCs

MSCs should meet the minimal criteria of the guidelines from

Mesenchymal and Tissue Stem Cell Committee of the ISCT including plastic adhesion, expression of specific surface markers (CD73, CD90, CD105, positive cells $\geq 95\%$; CD14, CD19, CD34, CD45, and HLA-DR, negative cells $\leq 2\%$) and capable of multilineage differentiation into adipocytes, osteoblasts and chondrocytes.

The surface marker expressions of HUCMSCs at P2, P5, and P10 were detected by Flow cytometry (FCM, BD facsaria™, USA). For each passage of HUCMSCs, a total of 2×10^5 cells per tube were incubated with the antibodies for 30 min. The phenotype of cells was analyzed by FlowJo V10 software.

A total of 1×10^5 cells/well of HUCMSCs at P2, P5, and P10 were inoculated in 6-wells plates for adipogenic and osteogenic differentiation. The adipogenesis differentiation kit (Gibco, A1007001) and osteogenesis differentiation kit (Gibco, A1007201) were changed every 3 days respectively. After 21 days, the osteogenesis and adipogenesis of HUCMSCs were evaluated by Oil Red O staining (Sigma-Aldrich) and Alizarin Red-S staining (Sigma-Aldrich, USA) respectively.

2.3. Immunomodulation assay

Increasingly evidence indicated that the most common immune-mediated indications in MSCs animal studies and human case were systemic lupus erythematosus (SLE), graft-versus-host disease (GVHD), and other diseases [38,39]. In this study, we isolated Peripheral blood mononuclear cells (PBMCs), which were co-cultured with HUCMSCs at P2, P5, and P10. The immunoregulatory effects of MSCs on Th1 (CD3⁺/CD8⁺/IFN- γ ⁺), Th17 (CD3⁺/CD8⁺/IL17⁺), and Tregs (CD4⁺/CD25⁺/Foxp3⁺) were determined by FCM (BD facsaria™, USA). About 5×10^4 cells/well of HUCMSCs were seeded in 12-well plates for Th1, Th17, and Tregs differentiation analysis. The detailed experimental methods and reagents could be referred to our previous studies [40].

2.4. Immunocytochemistry and Senescence-Associated β -galactosidase (SA- β -gal) staining

About 4×10^4 cells/well of HUCMSCs at P2, P5, and P10 were seed in 12-wells plates with glass coverslips and fixed with 4 % paraformaldehyde for 15 min. Then the HUCMSCs were stained by senescence β -galactosidase staining kit (Beyotime, China) according to the instruction of manufacturer. Cells were then permeabilized with 0.5 % Triton-X100 for 5 min and then blocked in bovine serum albumin for 1 h at room temperature. Subsequently, samples were incubated with the antibodies against pRPS6 (1:1000, 4858, Cell Signaling, USA) and Ki67 (1:200, ab279653, Abcam, USA) at 4°C overnight. We then used Goat anti-Rabbit IgG (H + L) highly cross-adsorbed secondary antibody, Alexa Fluor™ 488 (1:400, Invitrogen-A11034, USA), or Goat anti-Mouse IgG (H + L) highly cross-adsorbed secondary antibody, Alexa Fluor™ 568 (1:400, Invitrogen-A11031, USA). Nuclear staining was performed using DAPI mounting medium (ab104139, Abcam, UK), and micrographs were performed with a fluorescence microscope (Leica, Germany).

2.5. Western blot assay

HUCMSCs at P2, P5, and P10 were lysed with lysate buffer containing a protease inhibitor (Beyotime Biotechnology) and the concentrations were measured by BCA Protein Assay Kit (Beyotime Biotechnology). A total of 30 μ g HUCMSCs protein was loaded, separated by SDS/PAGE, and then transferred to a PVDF membrane. Next, blocked in 5 % BSA (Sigma-Aldrich), the membrane was incubated at 2–8°C overnight with following corresponding antibodies: anti-p21 (1:1000, CST, 2947S), anti-p16 (1:1000, Abcam, ab512433), anti-p53 (1:1000, CST, 2527S), and GAPDH (1:50,000; Proteintech Wuhan, China). Finally blots were detected with supersensitive ECL kit (Vazyme Biotech Co., Ltd) by scanner device (Tanon, 5200 Multi).

2.6. ResNext classification algorithm

CNN has been widely used in computer vision since Alex achieved the first place on ImageNet competition in 2012 [41]. For image classification task, CNN have surpassed humans in classification accuracy, so the CNN based method was proposed to complete HUCMSCs image classification in this study. So far, there have been many classification networks, such as AlexNet [42], VGGNet [43], GoogLeNet [44], ResNeXt [45]. ResNeXt could achieve a good of classification accuracy, so it had been used as the final neural network in this paper. The structure of ResNeXt network was shown in Fig. 1. First, we used a 7 x 7 convolutional layer and a maxpooling layer with stride of 2, which could quickly reduce the resolution of the image and the amount of computation. After that, we used multiple ResNext modules to extract features from images, and finally included a global average layer and a two-layer softmax classifier. The global average layer was used to aggregate feature information, and softmax classifier could output the probability of each classification category. Softmax function is as follows:

$$\text{softmax} : y_i = \frac{e^{x_i}}{\sum_{j=1}^n e^{x_j}} \quad (1)$$

Where y_i stands for the probability of belonging to category i , n represents a total of n categories. The softmax function converts the final output to a value between 0 and 1 to represent the probability of classification, which adds up to 1 for each category. We used cross-entropy function as our classification loss function.

2.7. Data availability

All data are presented as the mean value \pm standard deviation (SD) from at least three tests. The statistical analysis of data was performed by GraphPad Prism version 5.0 software. Comparison between multiple groups by one-way ANOVA was carried out to analyze data. $P < 0.05$ was considered significant.

3. Results

3.1. Characterization of HUCMSCs at different passages

We examined the morphology of HUCMSCs at different passages under an inverted microscope (Olympus, Japan). HUCMSCs at P2 and P5 were healthy spindle shaped, but those at P10 were enlarged and flat. The cell size of HUCMSCs at P10 was significantly increased compared with HUCMSCs at P2 and P5 (Fig. 2A). HUCMSCs at P2, P5, and P10 highly expressed markers CD73, CD90, and CD105 ($\geq 95\%$), and did not express CD14, CD19, CD34, CD45, or HLA-DR surface markers ($\leq 2\%$) (Fig. 2B). Subsequently, the osteogenic and adipogenic differentiation of HUCMSCs at P2, P5, and P10 were induced by certain induction medium and assayed by Alizarin Red and Oil Red O staining, respectively. The results showed that HUCMSCs at different passages have similar differentiation potential (Fig. 2C).

3.2. Immunomodulation effects of HUCMSCs at different passages

Many studies have been reported that MSCs possess excellent immunomodulatory potential via paracrine immune mediators or interactions with immune cells contributing to the therapeutic effects on various immune diseases [46]. PBMCs was isolated and cultured with different passages of each HUCMSCs strain to estimate the immunoregulation capability *in vitro*. HUCMSCs at P2, P5, and P10 could significantly diminish the proportion of CD3⁺/CD8⁺/IFN- γ + Th1 subpopulations and CD3⁺/CD8⁺/IL17 + Th17 subpopulations and greatly increased the proportion of CD4⁺/CD25⁺/Foxp3 + Treg subpopulations in PBMCs induced by IL-2 (Fig. 3A–F). Our findings showed that there was individual heterogeneity in immunomodulation among 3

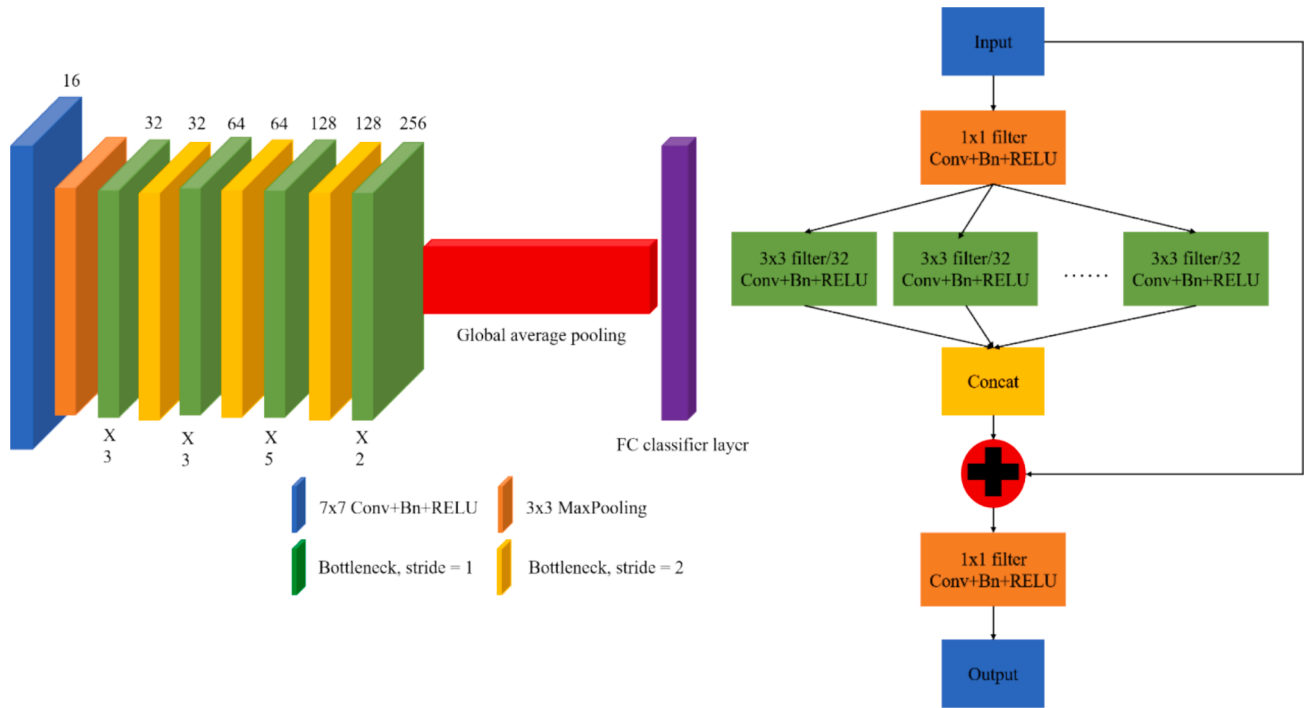


Fig. 1. The left diagram showed the classification network structure and the right diagram showed the specific implementation of its own bottleneck layer. The input is the output feature map from the previous layer. Suppose it is a channel number of n , the length and width are h and w respectively, we use a 1×1 convolution and reduce it to a feature with a channel number of $n/32$. The feature map is fed into 32 convolutional layers with $\text{stride} = 1$ respectively, and the output feature map is operated by concat, and the size of the feature map is still the same as the input. After that, we refer to the residual structure, add the input feature map element by element, and finally change the number of channels of the feature map through 1×1 convolution.

HUCMSCs, and the same HUCMSCs at different passages also have obvious differences in every aspect of immunomodulatory capability. For example, UC1 HUCMSCs had better immunoregulatory function than other two HUCMSCs. Interestingly, we found that HUCMSCs at P2 and P5 could markedly inhibited the activation and differentiation of CD4^+ T cells into Th17 subpopulations compared with HUCMSCs at P10. Above all, the results showed that the immune regulation function of HUCMSCs will decrease with the increase of cells passage *in vitro*.

3.3. Expansion of HUCMSCs induces senescence *in vitro*

To accurately assess the degree of cellular senescence across different generations, it may be necessary to evaluate multiple senescence markers. A comprehensive analysis of Ki67 and pRPS6 expression, along with the assessment of β -galactosidase activity, could facilitate the identification of senescence in HUCMSCs at P2, P5, and P10. The percentage of Ki67(−)pRPS6 (+)SA- β -gal (+) cells was enormously enhanced at P10 compared with P2 and P5 cells (Fig. 4A–B). To further validate our experimental observation, the proliferation ability of HUCMSCs at p2, p5 and p10 was detected by EDU staining. There was an obvious decrease in the percentage of EDU-positive HUCMSCs from P2 to P10 (Fig. 4C–D). We also examined the level of cellular senescence-related proteins p16, p21, and p53. All the three markers were markedly elevated at P10 HUCMSCs compared with those at P2 and P5 (Fig. 4E). We concluded that HUCMSCs could develop senescent phenotype during consecutive passaging expansion.

3.4. HUCMSCs image classification

3.4.1. Experiments setup

The deep learning framework used in this paper was Keras, which was a further encapsulated framework based on TensorFlow and had more advanced and convenient functions compared with TensorFlow [47]. The graphics card was a GTX1070TI. The network had been

trained and tested on a windows 10 desktop computer with 16 GB memory.

3.4.2. Image generation classification of HUCMSCs

In this study, we proposed an image analysis method of HUCMSCs based on CNN. For a given image of HUCMSCs, the generation of the cells in the image was predicted. We cultured 14 HUCMSCs strains and collected cell images from them. Among them, the cell images of 10 HUCMSCs strains were randomly selected to form the training set, the cell images of 2 HUCMSCs trains for the validation set, and the cell images of the remaining 2 HUCMSCs strains were used as the test set. The cell morphology of different passages for each strain was observed under an inverted microscope (Olympus, Japan). Several images (40 X) from generation P1 to P10 of these HUCMSCs were captured, and the resolution of each cell image was 2592x1944 pixels.

For an image of HUCMSCs, the amount of data for the task of predicting the generation or interval of the cells in the image was shown in Table 1 below:

For the task of predicting the generation or interval of the cells in, the category was 10 (a total of 10 generations). During training, the batch size was set as 8, and the stochastic gradient descent method was used for iteration. The learning rate, was initially 0.001, and then it would be drop 0.1 times if the accuracy of the validation set did not increase within 100 times (Fig. 5C).

During the test, in order to give a more accurate probability for each image, we cut the six regions of the image, namely the upper left, lower left, upper middle, lower middle, upper right and lower right, respectively to predict the probability of each generation. After averaging the probability of the six regions, the probability of the image belonging to each generation could be obtained. And for the task of measuring the generation of the cells, we post-processed the prediction results. Within the acceptable range, we allowed the prediction to give an interval of maximum probability. So we would go to sum the probabilities of each interval, and the interval with the highest probability is the prediction.

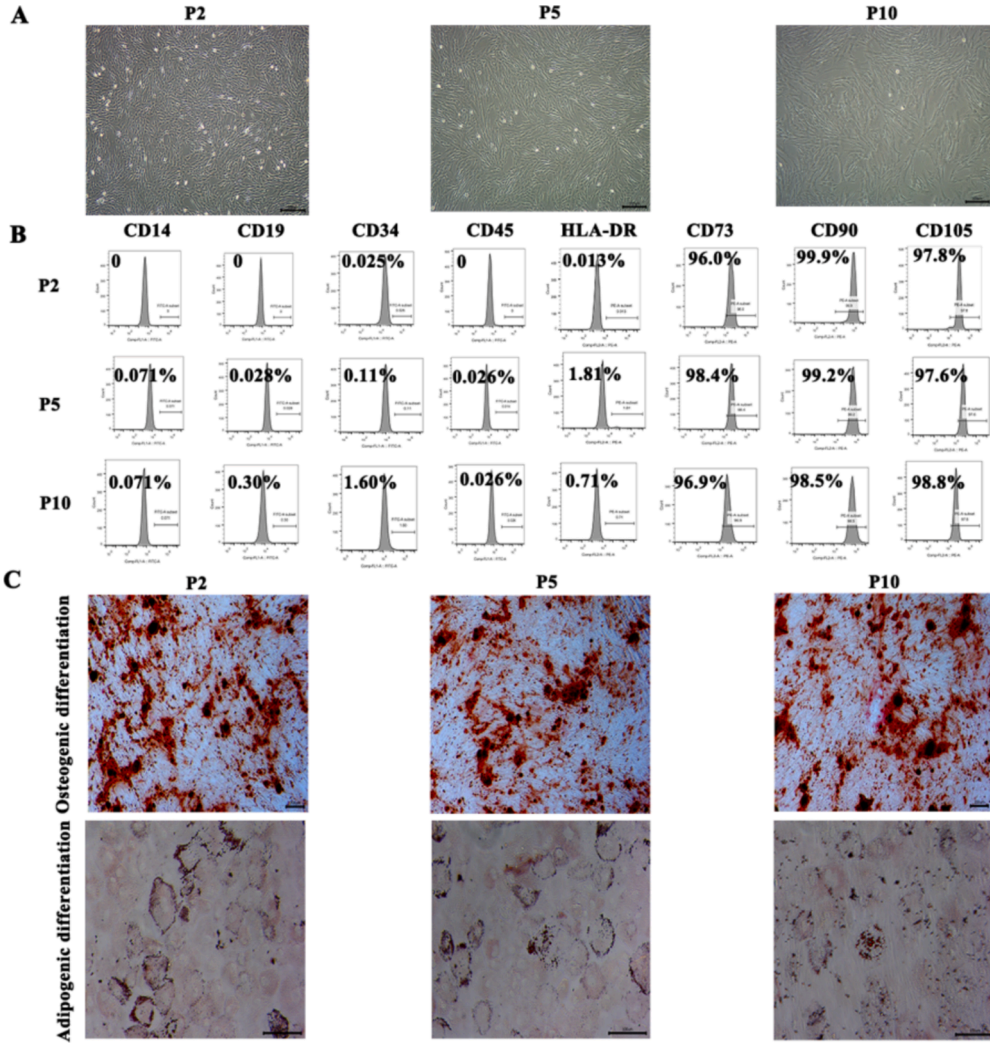


Fig. 2. Characterization of HUCMSCs at P2, P5, and P10. (A) HUCMSCs at different passage exhibited a similar morphology, but HUCMSCs at P10 showed an enlarged and flattened shape. (B) The surface markers of HUCMSCs at P2, P5, and P10 were analyzed. Flow cytometry was used to detect the surface markers in HUCMSCs, CD14, CD19, CD34, CD45, and HLA-DR were negative, while CD73, CD90, and CD105 were positive. (C) The osteogenic and adipogenic differentiation of HUCMSCs at P2, P5, and P10 were assayed by Alizarin Red (Scale bars = 200 μ m) and Oil Red O (Scale bars = 100 μ m) staining *in vitro*. (For interpretation of the references to color in this figure legend, the reader is referred to the web version of this article.)

The formula is:

$$\text{interval probabilities} = \frac{1}{m} \sum_{i=1}^{i+m} p_i, m = 1, \dots, 5, i = 1, \dots, n - m \quad (2)$$

Where m represents for the range of the interval, n is the total number of categories, and p represents the probability of category i predicted by the network (Fig. 5A).

For example, if we wanted to predict the most likely three generations of HUCMSCs corresponding to this image, we would sum the probabilities from the first generation to the third generation, which was regarded as the probability of belonging to the interval from the first generation to the third generation after obtaining the probability of each generation. Similarly, the summation of the probabilities from the second generation to the fourth generation was taken as the probabilities belonging to the second to fourth generation, and so on.

It was obvious that ResNeXt was accurated at 91.9 % in 3 generations and 99.5 % in 5 generations in validation set (Fig. 5B) and ResNeXt was accurated at 56.7 % in 3 generations and 91.0 % in 5 generations in test set (Fig. 5D). In addition, the accuracy of the network was 92.9 % for predicting which HUCMSCs strain in the training set the cells of image in validation set belonged to.

3.4.3. Classification of MSCs from different sources

The second part of this research was the classification of HUCMSCs and HBMMSCs. We define it as an image binary classification problem (Fig. 6A). The network structure was the ResNeXt described in 4.1, and the softmax of the last layer outputs the probabilities of 2 categories, and the loss function used the binary cross-entropy function. We took 1000 images using microscope as dataset, of which 500 were HUCMSCs and the other 500 were HBMMSCs. We take 70 % of the dataset as the training set with a total of 700 images, and 30 % as the test set with a total of 300 images, the specific data is shown in Table 2.

During training, we used the usual data augmentation for the training set, including color jitter, random flipping, random rotation, and translation. Then, a 448x448 sub-image is cropped from the center of the image and fed into the network for training. We used adam as the optimizer, the learning rate was set to 0.00001, the batch size was set to 8, After about 150 epochs of training, the network converges on the training dataset (Fig. 6B). Different from Section 4.4, during testing, a 448x448 image was cropped from the center of the image and fed directly into the network. In the study, our testing dataset consisted of 300 images, including 150 for HUCMSCs and 150 for HBMMSCs. The accuracy on the testing dataset reaches 90.2 %.

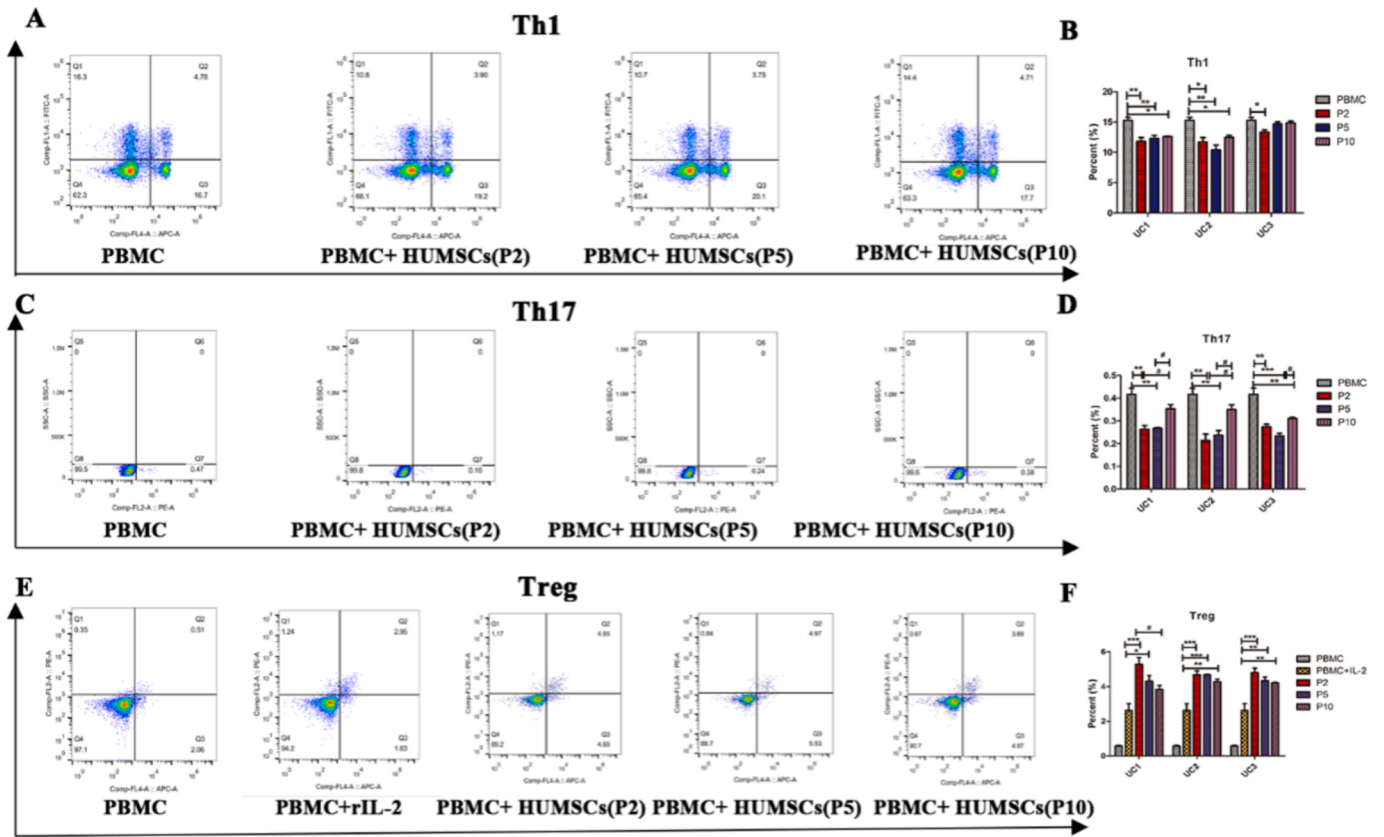


Fig. 3. Immunoregulation of HUCMSCs at p2, p5, and p10. There was remarkable individual heterogeneity in immunomodulation among 3 HUCMSCs, and had obvious differences in every aspect of immune regulation at P2, P5, and P10. (A-B) The $CD3^+/CD8^-/IFN-\gamma$ + Th1 cells were detected by FCM and quantitatively analyzed the data. (C-D) The $CD3^+/CD8^-/IL17$ + Th17 cells were detected by FCM and quantitatively analyzed the data. (E-F) The $CD4^+/CD25^+/Foxp3$ + Treg cells were detected by FCM and the data were quantitatively analyzed. Data represent as means \pm SD. * $p < 0.05$, ** $p < 0.01$, *** $p < 0.001$ and # $p < 0.05$ represents HUCMSCs at P2, P5, and P10 vs PBMC and HUCMSCs at P2 and P5 vs HUCMSCs at P10, respectively.

4. Discussion

In life, we can roughly judge what age a person is, and his/her physical condition from a person's appearance and body form. Similarly, cell aging will also company significant morphological changes, such as larger size, flat cell morphology, and poor refractive. Cell aging becomes serious with the increase of cell culture generation, and the aging cell biological activity gradually decreases. Therefore, the number of cell generations represented the quality of the cells to a certain extent. In this work, we proposed a deep learning method for image analysis of MSCs based on optical images of cellular morphology to identify the generation of HUCMSCs and classify the types of MSCs from different tissue sources such as HUCMSCs and HBMSCs. We used ResNeXt neural network as the classification network [41,48], which was improved on ResNet network, had a relatively deep network structure and could extract more features that were conducive to classification. We trained 14 HUCMSCs strains from generation P1 to P10, and extracted the cell image features accurately. In addition, the residual layer structure could directly transmit the signals from the bottom layer to the upper layer, and the network performance would not be worse as the depth increases, which can greatly improve the accuracy of cell recognition. In this method, we had completed predicting which generation the cells of the image belong to, predicting which generation the cells of the image in validation set belong to with an accuracy of 85.7 %. The accuracy of predicting within 3 generations was 91.9 %, while the accuracy rate of predicting within 5 generations was as high as 99.5 %. In test set, ResNeXt was accurate at 56.7 % in 3 generations and 91.0 % in 5 generations for untrained HUCMSCs. And for predicting which HUCMSCs strain in the training set the cells of image in validation set belong to, the

accuracy rate of the network reached 92.9 %. Meanwhile, the image classification accuracy for identifying HUCMSCs and HBMSCs was 90.2 %. This method successfully solved the problem that there was no effective method to identify the generation and strain of HUCMSCs, and identify the types of MSCs.

The convolutional neural network (CNN) use the convolution operations in the convolutional layer to extract features for classification task [49,50]. The difference with CNN is that these operators are all artificially designed, and CNN can automatically learn these parameters according to the back propagation of the error [51]. This makes it possible for complex features to be extracted by complex convolution kernels that cannot be designed by human beings, and the parameters in these convolution kernels are automatically adjusted by neural networks [52,53]. The feasibility of the convolutional neural network algorithm has been confirmed on the ImageNet data set [54,55]. At present, there are many convolutional neural networks that have excellent classification accuracy on ImageNet, such as VGGNet, GoogleNet, ResNet, and ResNeXt [56–59]. The research in this article showed that the ResNeXt network could be used to classify the generation and type of MSCs based on their optical images. The data source we used included cell images of 14 HUCMSCs strains from P1 to P10, which also included 14 HBMSCs strains images. Three models were trained with these data to predict which generation and strain of HUCMSCs and which type of MSCs were input into the images. In addition, cell image classification processing required millions of parameters that could be used for network adjustment. The number of cell lines we could use for training is limited, so we could greatly increase the training set data by dividing the original image into small sizes to reduce the amount of calculation and avoid over-fitting, so that the network had better performance on the training

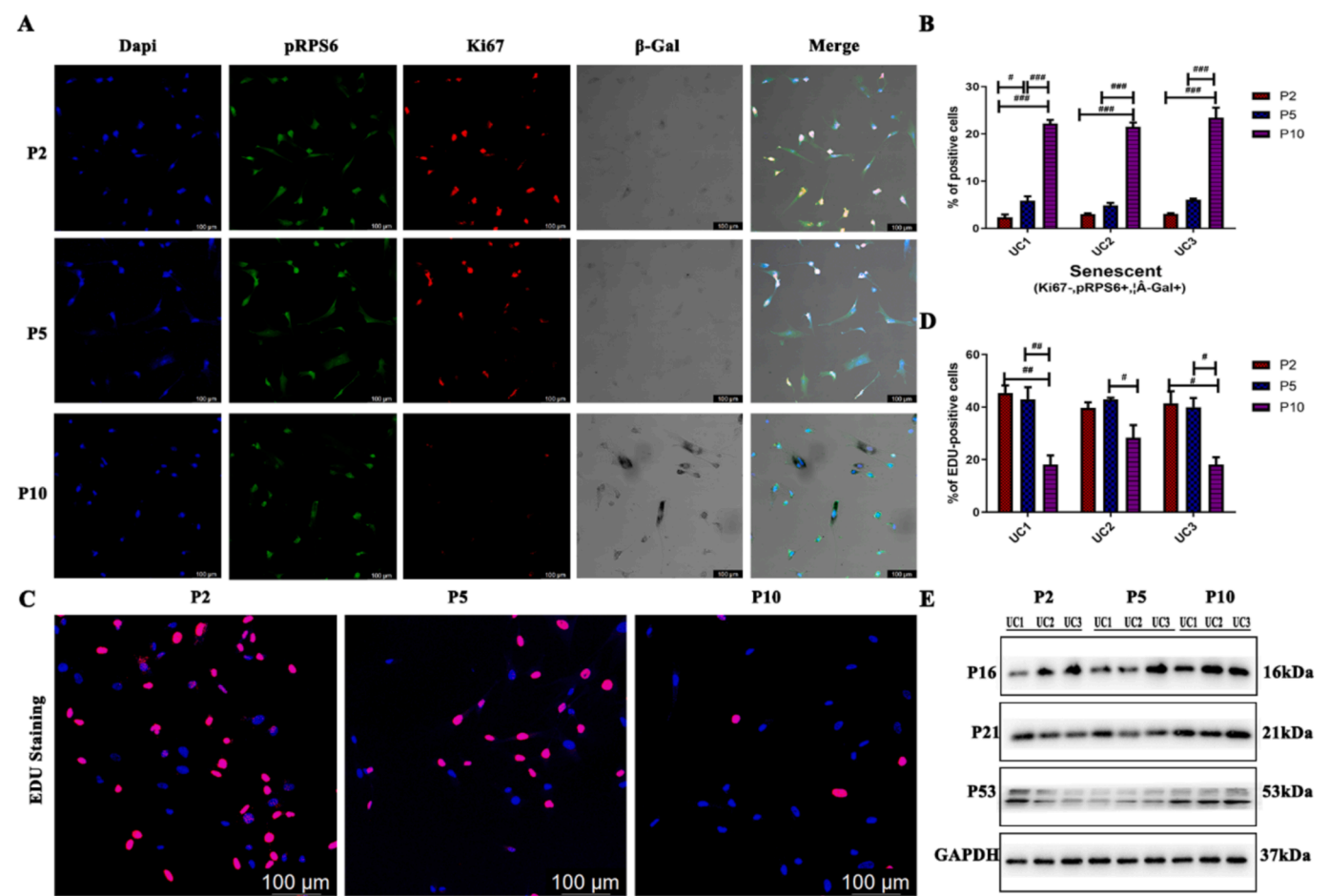


Fig. 4. Characterization of HUCMSCs replicative senescence. (A) Representative cell images of HUCMSCs at P2, P5, and P10 stained to identify DAPI, pRPS6, and Ki67 and to evaluate SA-β-gal activity. The Ki67(–)pRPS6(+)SA-β-gal(+) cells represented the senescence (Scale bars = 100 μm). (B) The Ki67(–)pRPS6(+)SA-β-gal(+) cells of HUCMSCs at P2, P5, and P10 were statistically analyzed. (C) Representative cell images of EDU staining in HUCMSCs at P2, P5, and P10 (Scale bars = 100 μm). (D) The EDU positive cells of HUCMSCs at P2, P5, and P10 were statistically analyzed. (E) The level of p16, p21 and p53 proteins in HUCMSCs at P2, P5, and P10 was analyzed by western blotting. Data represent as means ± SD. #*p* < 0.05, ##*p* < 0.01, ###*p* < 0.001 represents HUCMSCs at P2 and P5 vs HUCMSCs at P10.

Table 1
Data sets for the task of predicting the generation or interval of the cells in this image.

	P1	P2	P3	P4	P5	P6	P7	P8	P9	P10
Training dataset	156	154	144	139	141	116	117	113	105	101
Testing dataset	33	42	44	53	76	35	41	38	47	45

data set, and ensured that the network is more generalized. In the prediction, we also divided the original image into several blocks for individual prediction, and finally synthesized the prediction results of all the divided images to give the prediction result of the original image. Results proved that the ResNeXt network could well predict the generation and strain of HUCMSCs and the types of MSCs in the input images.

Stem cells as a new medicine is one of the most complex therapeutic products in the history of medicine. Unlike chemical molecular drugs with stable activity, stem cell biological activity is affected by various factors such as culture condition, generation number, donors and tissue heterogeneity [60]. MSCs-based therapy is a promising strategy for a variety of refractory diseases. Even when MSCs are cultured under standard conditions, as their passage increases *in vitro*, MSCs can easily become senescent, so that their beneficial effects are greatly diminished [61,62]. Senescent MSCs can secrete various factors such as inflammatory factors and other senescence-related secretory phenotypes (SASP), which further exacerbate cellular senescence, thereby reducing the

function of MSCs [63]. Senescent cells exhibit many biological characteristics including increased cell size, decreased cell proliferation rate, increased lysosome content characterized by SA-β-gal, and decreased immunomodulatory function [28,64]. The activity of p16, p21 and p53 is positively correlated with cellular senescence [65,66]. In our study, the results showed that HUCMSCs exhibited senescent phenotype during cell consecutive passaging expansion from P1 to P10 as evidenced by an increased cell size, increased Ki67(–)pRPS6(+)SA-β-gal(+) cells, decreased immune regulation function, a lower level of EDU, and elevation of the p16, p21 and p53 level. Thus, MSCs transplantation is best applied to cells within five generations, but until now there is no effective method for cell-consuming hospitals to monitor which generation the cells provided by company were in. The characteristic correlation between cell quality and morphology was analyzed based on biological characteristics and cell features. The quality assessment of MSCs included cell surface marker expressions, cell proliferation potential, cytokine secretion, immunoregulation, and multiple

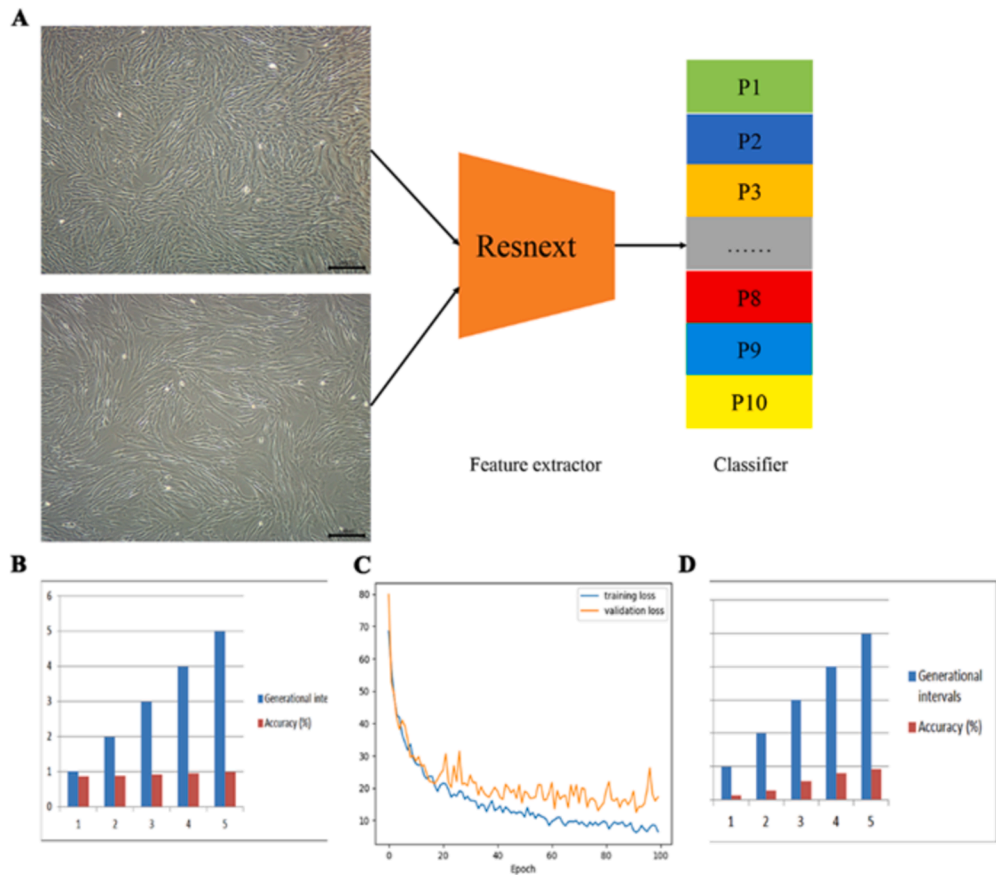


Fig. 5. The ResNeXt network predicted for the task of the generation or interval of HUCMSCs. (A) Image generation classification of HUCMSCs. (B) The accuracy of the task of predicting which interval the cells of this image in validation set were in. (C) Learning curve through the CNN training. Loss in the training data and validation data showed the process of training. (D) The accuracy of the task of predicting which interval the cells of this image.

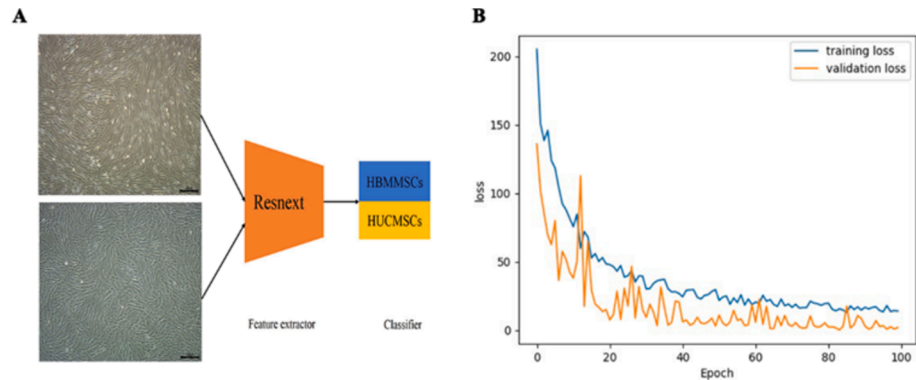


Fig. 6. The ResNeXt network predicted for the task of the types of MSCs. (A) Image classification of HUCMSCs and HBMMSCs. (B) Learning curve through the CNN training of HUCMSCs and HBMMSCs. Loss in the training data and validation data showed the process of training.

Table 2
HUCMSCs and HBMMSCs image classification dataset.

	Training set	Testing set
HUCMSCs	350	150
HBMMSCs	350	150
Total	700	300

differentiation potential. The cellular image features of different biological activity were utilized to monitor the quality of cells through their images. A Deep learning method is used to build a system to enable

customers to determine which generation the cells provided by the manufacturer belong to only through cell pictures. In other words, simply through this system we have mastered the capability to roughly judge the quality of the stem cell product we used, without requiring a complex and systematic quality evaluation of the cell product. In addition, the manufacturer can also use it to perform cell traceability, added a traceability method other than tags. Therefore, this method could be widely used in clinical application of stem cell-based therapy and in cell producing of manufacturer.

Although this study has achieved the expected results in the generation and the types identification of MSCs, there are still some shortcomings need to be further improved. Combining the content described

in this article, the following improvement ideas are proposed and the future work direction is prospected. First, the data set in this article was all derived from 14 HUCMSCs strains, which may make the training set too single and the size of samples was not very large, which easily caused the generalization ability of the cell recognition network to weaken. Therefore, to solve this problem, we should expand the data set of HUCMSCs strains more in the future, which is expected to further improve the accuracy of the network in identifying MSCs.

Secondly, all the data sets in this paper were derived from HUCMSCs and HBMMSCs, and the types of cells were limited. Currently, HUCMSCs and HBMMSCs are two commonly used types of MSCs in stem cells research. Observed by inverted phase contrast microscope, the cell morphology of HUCMSCs and HBMMSCs was significantly different. The cell morphology of HUCMSCs was long spindle-shaped, closely arranged, and grows in parallel or spiral shape, while the cell morphology of HBMMSCs was more slender, thick in the middle, slender at both ends, and less antennae. In this study, the ResNeXt network we used could predict HUCMSCs with an accuracy of 90.2 %. However, the morphology of HUCMSCs was similar to that of human gingival and dental pulp derived MSCs, which are fibroblast like, long fusiform and closely arranged [67,68]. This method may not be able to distinguish cell types derived from different tissue, lacking a good cell type specificity when identify a variety of MSCs. Therefore, we should train other types of MSCs derived from more different tissues to deal with image classification problems.

In conclusion, we showed that generation number of clinic-grade MSCs during their expansion correlated with the manifestation of cellular quality and senescence-associated markers. We have developed an automated image analysis method based on the morphology of MSCs to recognize the generation numbers of cultured MSCs during their expansion, providing a helpful tool for quick cellular quality screening in MSCs-based therapy.

Ethics approval and consent to participate

This study was approved by the Research Ethics Board of Nanjing Drum Tower Hospital, Affiliated Hospital of Medical School, Nanjing University (No.2020AE01031). Human umbilical cord and bone marrow tissues were obtained from the Department of Obstetrics and Gynecology, Nanjing Drum Tower Hospital. All donors signed informed consent.

Author contributions

Bin Wang, Xiaoli Mai and Yang Chen conceived and designed the study. Liudi Wang, Tianyun Gao and Yuanyuan Xie performed the experiments. Haijie Zhang, Jianwei Chen and Xiangtian Xue analyzed the data. Liudi Wang and Haijie Zhang wrote the manuscript through fruitful discussions with and supervision by Bin Wang, Xiaoli Mai and Yang Chen.

CRedit authorship contribution statement

Liudi Wang: Writing – review & editing, Writing – original draft, Data curation. **Haijie Zhang:** Software, Data curation. **Jianwei Chen:** Writing – original draft, Data curation. **Xiangtian Xue:** Data curation. **Yang Chen:** Conceptualization. **Tianyun Gao:** Methodology. **Yuanyuan Xie:** Methodology. **Xiaoli Mai:** Writing – review & editing, Conceptualization. **Bin Wang:** Writing – review & editing, Conceptualization.

Funding

This study was supported by the National Key Research and Development Program of China (2017YFA0104300, and 2024YFA1107200), National Natural Science Foundation of China (NSFC) [81571213, 82070459 and 82270,701 (Bin Wang), 82472048 (Xiaoli Mai), and

81800583 (Yuanyuan Xie)].

Declaration of competing interest

The authors declare that they have no known competing financial interests or personal relationships that could have appeared to influence the work reported in this paper.

Acknowledgments

In this study, we appreciate the donors for their tissue donations.

Data availability

Data will be made available on request.

References

- [1] M. Liu, J. Chen, H. Huang, Y. Zeng, X. Feng, M. Shi, Lkb1 is an important regulator of Treg differentiation and proliferation of amniotic mesenchymal stem cells, *Biochem. Biophys. Res. Commun.* 521 (2020) 434–440, <https://doi.org/10.1016/j.bbrc.2019.09.129>.
- [2] T. Nagamura-Inoue, H. He, Umbilical cord-derived mesenchymal stem cells: their advantages and potential clinical utility, *World J. Stem Cells* 6 (2014) 195–202, <https://doi.org/10.4252/wjsc.v6.i2.195>.
- [3] W. Yan, S. Diao, Z. Fan, The role and mechanism of mitochondrial functions and energy metabolism in the function regulation of the mesenchymal stem cells, *Stem Cell Res. Ther* 12 (2021) 140, <https://doi.org/10.1186/s13287-021-02194-z>.
- [4] M. Dominici, K. Le Blanc, I. Mueller, I. Slaper-Cortenbach, F. Marini, D. Krause, R. Deans, A. Keating, D. Prockop, E. Horwitz, Minimal criteria for defining multipotent mesenchymal stromal cells. The international society for cellular therapy position Statement, *Cytotherapy* 8 (2006) 315–317, <https://doi.org/10.1080/14653240600855905>.
- [5] L. De Chiara, E.S. Famulari, S. Fagoonee, S.K.M. van Daalen, S. Buttiglieri, A. Revelli, E. Tolosano, L. Silengo, A.M.M. van Pelt, F. Altruda, Characterization of human mesenchymal stem cells isolated from the testis, *Stem Cells Int.* 2018 (2018) 4910304, <https://doi.org/10.1155/2018/4910304>.
- [6] E. Hohmann, Editorial Commentary: Stem Cells. They Are in the Fat Tissue, Bone Marrow, and Even in the Synovial Fluid of the Knee Joint, *Arthroscopy: the journal of arthroscopic & related surgery: official publication of the Arthroscopy Association of North America and the International Arthroscopy Association* 37 (2021) 901–902, <https://doi.org/10.1016/j.arthro.2020.12.216>.
- [7] K.K.S. Venugopal, K.S. Rai, V.B. Pinnelli, B.M. Kutty, A. Dhanushkodi, Neuroprotection by human dental pulp mesenchymal stem cells: from billions to nano, *Current Gene Therapy* 18 (2018) 307–323, <https://doi.org/10.2174/1566523218666180913152615>.
- [8] C. Vidoni, A. Ferraresi, E. Secomandi, L. Vallino, C. Gardin, B. Zavan, C. Mortellaro, C. Isidoro, Autophagy drives osteogenic differentiation of human gingival mesenchymal stem cells, *Cell Commun. Signal* 17 (2019) 98, <https://doi.org/10.1186/s12964-019-0414-7>.
- [9] H. Zhou, J. Zhu, M. Liu, Q. Wu, N. Dong, Role of the protease corin in chondrogenic differentiation of human bone marrow-derived mesenchymal stem cells, *J. Tissue Eng. Regen. Med.* 12 (2018) 973–982, <https://doi.org/10.1002/term.2514>.
- [10] L. Hu, C. Yin, F. Zhao, A. Ali, J. Ma, A. Qian, Mesenchymal stem cells: cell fate decision to osteoblast or adipocyte and application in osteoporosis treatment, *Int. J. Mol. Sci.* 19 (2018), <https://doi.org/10.3390/ijms19020360>.
- [11] M.C. Ciuffreda, G. Malpasso, P. Musaro, V. Turco, M. Gnechi, Protocols for in vitro differentiation of human mesenchymal stem cells into osteogenic, chondrogenic and adipogenic lineages, *Methods Mol Biol* 1416 (2016) 149–158, https://doi.org/10.1007/978-1-4939-3584-0_8.
- [12] V. Suryadevara, A.D. Hudgins, A. Rajesh, A. Pappalardo, A. Karpova, A.K. Dey, A. Hertz, A. Agudelo, A. Rocha, B. Soygar, B. Schilling, C.M. Carver, C. Aguayo-Mazzucato, D.J. Baker, D.A. Bernlohr, D. Jurk, D.B. Mangarova, E.M. Quardokus, E.A.L. Enninga, E.L. Schmidt, F. Chen, F.E. Duncan, F. Cambuli, G. Kaur, G. A. Kuchel, G. Lee, H.E. Daldrup-Link, H. Martini, H. Phatnani, I.M. Al-Naggar, I. Rahman, J. Nie, J.F. Passos, J.C. Silverstein, J. Campisi, J. Wang, K. Iwasaki, K. Barbosa, K. Metis, K. Nernekli, L.J. Niedernhofer, L. Ding, L. Wang, L.C. Adams, L. Ruiyang, M.L. Doolittle, M.G. Tenenche, M.J. Schafer, M. Xu, M. Hajipour, M. Boroumand, N. Basisty, N. Sloan, N. Slavov, O. Kuksenko, P. Robson, P. T. Gomez, P. Vasilikos, P.D. Adams, P. Carapeto, Q. Zhu, R. Ramasamy, R. Perez-Lorenzo, R. Fan, R. Dong, R.R. Montgomery, S. Shaikh, S. Vickovic, S. Yin, S. Kang, S. Suvakov, S. Khosla, V.D. Garovic, V. Menon, Y. Xu, Y. Song, Y. Suh, Z. Dou, N. Neretti, SenNet recommendations for detecting senescent cells in different tissues, *Nat. Rev. Mol. Cell Biol* 25 (2024) 1001–1023, <https://doi.org/10.1038/s41580-024-00738-8>.
- [13] J.R. Mauney, D.L. Kaplan, V. Volloch, Matrix-mediated retention of osteogenic differentiation potential by human adult bone marrow stromal cells during ex vivo expansion, *Biomaterials* 25 (2004) 3233–3243, <https://doi.org/10.1016/j.biomaterials.2003.10.005>.

- [14] K. Stenderup, J. Justesen, C. Clausen, M. Kassem, Aging is associated with decreased maximal life span and accelerated senescence of bone marrow stromal cells, *Bone* 33 (2003) 919–926, <https://doi.org/10.1016/j.bone.2003.07.005>.
- [15] A. Stolzinger, A. Scutt, Age-related impairment of mesenchymal progenitor cell function, *Aging Cell* 5 (2006) 213–224, <https://doi.org/10.1111/j.1474-9726.2006.00213.x>.
- [16] A. Banfi, G. Bianchi, R. Notaro, L. Luzzatto, R. Cancedda, R. Quarto, Replicative aging and gene expression in long-term cultures of human bone marrow stromal cells, *Tissue Eng* 8 (2002) 901–910, <https://doi.org/10.1089/107632702320934001>.
- [17] M. Liu, H. Lei, P. Dong, X. Fu, Z. Yang, Y. Yang, J. Ma, X. Liu, Y. Cao, R. Xiao, Adipose-derived mesenchymal stem cells from the elderly exhibit decreased migration and differentiation abilities with senescent properties, *Cell Transplant.* 26 (2017) 1505–1519, <https://doi.org/10.1177/0963689717721221>.
- [18] P. Sousa-Victor, S. Gutarra, L. García-Prat, J. Rodríguez-Ubveira, L. Ortet, V. Ruiz-Bonilla, M. Jardi, E. Ballestar, S. González, A.L. Serrano, E. Perdiguerro, P. Muñoz-Cánoves, Geriatric muscle stem cells switch reversible quiescence into senescence, *Nature* 506 (2014) 316–321, <https://doi.org/10.1038/nature13013>.
- [19] L. García-Prat, M. Martínez-Vicente, E. Perdiguerro, L. Ortet, J. Rodríguez-Ubveira, E. Rebollo, V. Ruiz-Bonilla, S. Gutarra, E. Ballestar, A.L. Serrano, M. Sandri, P. Muñoz-Cánoves, Autophagy maintains stemness by preventing senescence, *Nature* 529 (2016) 37–42, <https://doi.org/10.1038/nature16187>.
- [20] D.I. Benjamin, P. Both, J.S. Benjamin, C.W. Nutter, J.H. Tan, J. Kang, L. A. Machado, J.D.D. Klein, A. de Morree, S. Kim, L. Liu, H. Dulay, L. Feraboli, S. M. Louie, D.K. Nomura, T.A. Rando, Fasting induces a highly resilient deep quiescent state in muscle stem cells via ketone body signaling, *CellMetab* 34 (2022) 902–918.e906, <https://doi.org/10.1016/j.cmet.2022.04.012>.
- [21] F. Rodier, J. Campisi, Four faces of cellular senescence, *J Cell Biol* 192 (2011) 547–556, <https://doi.org/10.1083/jcb.201009094>.
- [22] M.V. Blagosklonny, Rapamycin, proliferation and geroconversion to senescence, *Cell Cycle* 17 (2018) 2655–2665, <https://doi.org/10.1080/15384101.2018.1554781>.
- [23] S. Sengupta, T.R. Peterson, M. Laplante, S. Oh, D.M. Sabatini, mTORC1 controls fasting-induced ketogenesis and its modulation by ageing, *Nature* 468 (2010) 1100–1104, <https://doi.org/10.1038/nature09584>.
- [24] M.V. Blagosklonny, Cell cycle arrest is not yet senescence, which is not just cell cycle arrest: terminology for TOR-driven aging, *Aging (Albany NY)* 4 (2012) 159–165, [10.18632/aging.100443](https://doi.org/10.18632/aging.100443).
- [25] J.T. Park, Y.S. Lee, K.A. Cho, S.C. Park, Adjustment of the lysosomal-mitochondrial axis for control of cellular senescence, *Ageing Res. Rev.* 47 (2018) 176–182, <https://doi.org/10.1016/j.arr.2018.08.003>.
- [26] F. Debacq-Chainiaux, J.D. Erusalimsky, J. Campisi, O. Toussaint, Protocols to detect senescence-associated beta-galactosidase (SA-beta-gal) activity, a biomarker of senescent cells in culture and in vivo, *Nat. Protoc.* 4 (2009) 1798–1806, <https://doi.org/10.1038/nprot.2009.191>.
- [27] J. Wu, H. Ding, G. Wang, Y. Zhou, [The frequency features and application of edge detection differential operators in medical image], *Sheng wu yi xue gong cheng xue za zhi* 22 (2005) 82–85.
- [28] N. Alessio, D. Aprile, S. Cappabianca, G. Peluso, G. Di Bernardo, U. Galderisi, Different stages of quiescence, senescence, and cell stress identified by molecular algorithm based on the expression of Ki67, RPS6, and beta-galactosidase activity, *Int. J. Mol. Sci.* 22 (2021), <https://doi.org/10.3390/ijms22063102>.
- [29] T. Kuilman, C. Michaloglou, W.J. Mooi, D.S. Peeper, The essence of senescence, *Genes Dev.* 24 (2010) 2463–2479, <https://doi.org/10.1101/gad.1971610>.
- [30] J. Campisi, F. d'Adda di Fagagna, Cellular senescence: when bad things happen to good cells, *Nat. Rev. Mol. Cell Biol* 8 (2007) 729–740, <https://doi.org/10.1038/nrm2233>.
- [31] L. Barkholt, E. Flory, V. Jekerle, S. Lucas-Samuel, P. Ahnert, L. Bisset, D. Buscher, W. Fibbe, A. Foussat, M. Kwa, O. Lantz, R. Maculaitis, T. Palomaki, C.K. Schneider, L. Sensebe, G. Tachdjian, K. Tarte, L. Tosca, P. Salmikangas, Risk of tumorigenicity in mesenchymal stromal cell-based therapies—bridging scientific observations and regulatory viewpoints, *Cytotherapy* 15 (2013) 753–759, <https://doi.org/10.1016/j.jcyt.2013.03.005>.
- [32] A.R. Davalos, J.P. Coppe, J. Campisi, P.Y. Desprez, Senescent cells as a source of inflammatory factors for tumor progression, *Cancer Metastasis Rev.* 29 (2010) 273–283, <https://doi.org/10.1007/s10555-010-9220-9>.
- [33] Y. Xie, W. Liu, S. Liu, L. Wang, D. Mu, Y. Cui, Y. Cui, B. Wang, The quality evaluation system establishment of mesenchymal stromal cells for cell-based therapy products, *Stem Cell Res. Ther.* 11 (2020) 176, <https://doi.org/10.1186/s13287-020-01696-6>.
- [34] S. Soffer, A. Ben-Cohen, O. Shimon, M.M. Amitai, H. Greenspan, E. Klang, Convolutional neural networks for radiologic images: a Radiologist's guide, *Radiology* 290 (2019) 590–606, <https://doi.org/10.1148/radiol.2018180547>.
- [35] D. Abdelhafiz, C. Yang, R. Ammar, S. Nabavi, Deep convolutional neural networks for mammography: advances, challenges and applications, *BMC Bioinf.* 20 (2019) 281, <https://doi.org/10.1186/s12859-019-2823-4>.
- [36] D.X. Zhou, Theory of deep convolutional neural networks: downsampling, *Neural Networks: Off. J. Int. Neural Network Soc.* 124 (2020) 319–327, <https://doi.org/10.1016/j.neunet.2020.01.018>.
- [37] Z. Dashdorj, M. Song, An application of convolutional neural networks with salient features for relation classification, *BMC Bioinf.* 20 (2019) 244, <https://doi.org/10.1186/s12859-019-2808-3>.
- [38] M. Gupta, A. Tieu, M. Slobodian, R. Shorr, D. Burger, M.M. Lalu, D.S. Allan, Preclinical studies of MSC-derived extracellular vesicles to treat or prevent graft versus host disease: a systematic review of the literature, *Stem Cell Rev. Rep.* 17 (2021) 332–340, <https://doi.org/10.1007/s12015-020-10058-x>.
- [39] A. Li, F. Guo, Q. Pan, S. Chen, J. Chen, H.F. Liu, Q. Pan, Mesenchymal stem cell therapy: hope for patients with systemic lupus erythematosus, *Front Immunol* 12 (2021) 728190, <https://doi.org/10.3389/fimmu.2021.728190>.
- [40] Y. Xie, S. Liu, L. Wang, H. Yang, C. Tai, L. Ling, L. Chen, S. Liu, B. Wang, Individual heterogeneity screened umbilical cord-derived mesenchymal stromal cells with high Treg promotion demonstrate improved recovery of mouse liver fibrosis, *Stem Cell Res. Ther.* 12 (2021) 359, <https://doi.org/10.1186/s13287-021-02430-6>.
- [41] L. Blaivas, M. Blaivas, Are convolutional neural networks trained on imagenet images wearing rose-colored glasses?: a quantitative comparison of imagenet, computed tomographic, magnetic resonance, chest X-ray, and point-of-care ultrasound images for quality, *J. Ultrasound Med.* 40 (2021) 377–383, <https://doi.org/10.1002/jum.15413>.
- [42] H. Hashimoto, S. Kameda, H. Maezawa, S. Oshino, N. Tani, H.M. Khoo, T. Yanagisawa, T. Yoshimine, H. Kishima, M. Hirata, A swallowing decoder based on deep transfer learning: AlexNet classification of the intracranial electrocorticogram, *Int. J. Neural Syst.* 31 (2021) 2050056, <https://doi.org/10.1142/S0129065720500562>.
- [43] Z. Liu, Y. Cao, Y. Li, X. Xiao, Q. Qiu, M. Yang, Y. Zhao, L. Cui, Automatic diagnosis of fungal keratitis using data augmentation and image fusion with deep convolutional neural network, *Comput. Methods Programs Biomed.* 187 (2020) 105019, <https://doi.org/10.1016/j.cmpb.2019.105019>.
- [44] L. Balagourouchetty, J.K. Pragatheeswaran, B. Pottakkat, GoogLeNet-Based Ensemble FCNet Classifier for Focal Liver Lesion Diagnosis, *IEEE journal of biomedical and health informatics* 24 (2020) 1686–1694, <https://doi.org/10.1109/JBHI.2019.2942774>.
- [45] Y. Chen, T. Yang, C. Li, Y. Zhang, A binarized segmented ResNet based on edge computing for re-identification, *Sensors (Basel)* 20 (2020), <https://doi.org/10.3390/s20236902>.
- [46] Y. Shi, Y. Wang, Q. Li, K. Liu, J. Hou, C. Shao, Y. Wang, Immunoregulatory mechanisms of mesenchymal stem and stromal cells in inflammatory diseases, *Nat. Rev. Nephrol.* 14 (2018) 493–507, <https://doi.org/10.1038/s41581-018-0023-5>.
- [47] L. Rampasek, A. Goldenberg, TensorFlow: Biology's gateway to deep learning? *CellSyst* 2 (2016) 12–14, <https://doi.org/10.1016/j.cels.2016.01.009>.
- [48] J. Zhang, Z. Liu, B. Du, J. He, G. Li, D. Chen, Binary tree-like network with two-path Fusion Attention Feature for cervical cell nucleus segmentation, *Comput. Biol. Med.* 108 (2019) 223–233, <https://doi.org/10.1016/j.compbiomed.2019.03.011>.
- [49] O. Durr, B. Sick, Single-cell phenotype classification using deep convolutional neural networks, *J. Biomol. Screen.* 21 (2016) 998–1003, <https://doi.org/10.1177/1087057116631284>.
- [50] H. Li, F. Pang, Y. Shi, Z. Liu, Cell dynamic morphology classification using deep convolutional neural networks, *Cytometry, Part A: J. Int. Soc. Analytical Cytol.* 93 (2018) 628–638, <https://doi.org/10.1002/cyto.a.23490>.
- [51] P. He, Y. Fan, B. Pan, Y. Zhu, J. Liu, D. Zhu, Calibration and verification of dynamic particle flow parameters by the back-propagation neural network based on the genetic algorithm: recycled polyurethane powder, *Materials (Basel)* 12 (2019), <https://doi.org/10.3390/ma12203350>.
- [52] H.J. Jiang, Z.H. You, Y.A. Huang, Predicting drug-disease associations via sigmoid kernel-based convolutional neural networks, *J. Transl. Med.* 17 (2019) 382, <https://doi.org/10.1186/s12967-019-2127-5>.
- [53] C.I. Patel, D. Labana, S. Pandya, K. Modi, H. Ghayvat, M. Awais, Histogram of oriented gradient-based fusion of features for human action recognition in action video sequences, *Sensors (Basel)* 20 (2020), <https://doi.org/10.3390/s20247299>.
- [54] P. Lakhani, B. Sundaram, Deep learning at chest radiography: automated classification of pulmonary tuberculosis by using convolutional neural networks, *Radiology* 284 (2017) 574–582, <https://doi.org/10.1148/radiol.2017162326>.
- [55] X. Shu, L. Zhang, Z. Wang, Q. Lv, Z. Yi, Deep neural networks with region-based pooling structures for mammographic image classification, *IEEE Trans. Med. Imaging* 39 (2020) 2246–2255, <https://doi.org/10.1109/TMI.2020.2968397>.
- [56] F. He, T. Liu, D. Tao, Why ResNet Works? Residuals Generalize, *IEEE Transactions on Neural Networks and Learning Systems* 31 (2020) 5349–5362, <https://doi.org/10.1109/TNNLS.2020.2966319>.
- [57] J. Wang, K. Sun, T. Cheng, B. Jiang, C. Deng, Y. Zhao, D. Liu, Y. Mu, M. Tan, X. Wang, W. Liu, B. Xiao, Deep high-resolution representation learning for visual recognition, *IEEE Trans. Pattern Anal. Mach. Intell.* 43 (2021) 3349–3364, <https://doi.org/10.1109/TPAMI.2020.2983686>.
- [58] S.M. Anwar, M. Majid, A. Qayyum, M. Awais, M. Alnowami, M.K. Khan, Medical image analysis using convolutional neural networks: a review, *J. Med. Syst.* 42 (2018) 226, <https://doi.org/10.1007/s10916-018-1088-1>.
- [59] E. Shelhamer, J. Long, T. Darrell, Fully convolutional networks for semantic segmentation, *IEEE Trans. Pattern Anal. Mach. Intell.* 39 (2017) 640–651, <https://doi.org/10.1109/TPAMI.2016.2572683>.
- [60] Z. Cui, H. Wei, C. Goding, R. Cui, Stem cell heterogeneity, plasticity, and regulation, *Life Sci* 334 (2023) 122240, <https://doi.org/10.1016/j.lfs.2023.122240>.
- [61] Y.H. Chao, C.T. Peng, H.J. Harn, C.K. Chan, K.H. Wu, Poor potential of proliferation and differentiation in bone marrow mesenchymal stem cells derived from children with severe aplastic anemia, *Ann. Hematol.* 89 (2010) 715–723, <https://doi.org/10.1007/s00277-009-0892-6>.
- [62] J. Kim, Y. Kim, H. Choi, A. Kwon, D.W. Jekal, S. Lee, W. Jang, H. Chae, J.R. Kim, J.M. Kim, M. Kim, Ubiquitin C decrement plays a pivotal role in replicative senescence of bone marrow mesenchymal stromal cells, *Cell Death Dis.* 9 (2018) 139, <https://doi.org/10.1038/s41419-017-0032-5>.
- [63] J.Y. Lee, K.R. Yu, B.C. Lee, I. Kang, J.J. Kim, E.J. Jung, H.S. Kim, Y. Seo, S.W. Choi, K.S. Kang, GATA4-dependent regulation of the secretory phenotype via MCP-1

- underlies lamin A-mediated human mesenchymal stem cell aging, *Exp. Mol. Med.* 50 (2018) 1–12, <https://doi.org/10.1038/s12276-018-0092-3>.
- [64] V.V. Lunyak, A. Amaro-Ortiz, M. Gaur, Mesenchymal stem cells secretory responses: senescence messaging secretome and immunomodulation perspective, *Front. Genet.* 8 (2017) 220, <https://doi.org/10.3389/fgene.2017.00220>.
- [65] C. Jiang, G. Liu, T. Luckhardt, V. Antony, Y. Zhou, A.B. Carter, V.J. Thannickal, R. M. Liu, Serpine 1 induces alveolar type II cell senescence through activating p53-p21-Rb pathway in fibrotic lung disease, *Aging Cell* 16 (2017) 1114–1124, <https://doi.org/10.1111/acer.12643>.
- [66] D. Kusumoto, T. Seki, H. Sawada, A. Kunitomi, T. Katsuki, M. Kimura, S. Ito, J. Komuro, H. Hashimoto, K. Fukuda, S. Yuasa, Anti-senescent drug screening by deep learning-based morphology senescence scoring, *Nat. Commun.* 12 (2021) 257, <https://doi.org/10.1038/s41467-020-20213-0>.
- [67] T. Lin, W.Q. Zhao, Y.L. Lu, Y.Y. Liu, L.R. Bao, Y. Wu, Human umbilical cord mesenchymal stem cells co-cultured with dental pulp cells in vitro and its effect on cell biological behaviors, *Shanghai Kou Qiang Yi Xue* 27 (2018) 365–369.
- [68] C. Jeon, K.C. Oh, K.H. Park, H.S. Moon, Effects of ultraviolet treatment and alendronate immersion on osteoblast-like cells and human gingival fibroblasts cultured on titanium surfaces, *Sci. Rep.* 9 (2019) 2581, <https://doi.org/10.1038/s41598-019-39355-3>.